The Astrophysical Journal Letters, 870:L9 (11pp), 2019 January 1 https://doi.org/10.3847/2041-8213/aaf8b9

SOFIA Far-infrared Imaging Polarimetry of M82 and NGC 253: Exploring the Supergalactic Wind

Terry Jay Jones[1], C. Darren Dowell[2], Enrique Lopez Rodriguez[3,4], Ellen G. Zweibel[5], Marc Berthoud[6,7], David T. Chuss[8], Paul F. Goldsmith[2], Ryan T. Hamilton[9], Shaul Hanany[10], Doyal A. Harper[7,11], Alex Lazarian[5], Leslie W. Looney[12], Joseph M. Michail[8,13], Mark R. Morris[14], Giles Novak[15], Fabio P. Santos[16], Kartik Sheth[17], Gordon J. Stacey[18], Johannes Staguhn[19,20], Ian W. Stephens[21], Konstantinos Tassis[22,23], Christopher Q. Trinh[24], C. G. Volpert[6], Michael Werner[2], and Edward J. Wollack[20]
(HAWC+ Science Team)

[1] Minnesota Institute for Astrophysics Universtity of Minnesota 116 Church Street SE, Minneapolis, MN 55455, USA; tjj@astro.umn.edu
[2] NASA Jet Propulsion Laboratory, California Institute of Technology, 4800 Oak Grove Drive, Pasadena, CA 91109, USA
[3] SOFIA Science Center/Universities Space Research Association
[4] NASA Ames Research Center, M.S. N232-12, Moffett Field, CA 94035, USA
[5] Department of Astronomy, University of Wisconsin, Madison, WI 53706, USA
[6] University of Chicago, Chicago, IL 60637, USA
[7] Yerkes Observatory, Williams Bay, WI, USA
[8] Department of Physics, Villanova University, 800 E. Lancaster Avenue, Villanova, PA 19085, USA
[9] Lowell Observatory, 1400 W Mars Hill Road, Flagstaff, AZ 86001, USA
[10] School of Physics and Astronomy, University of Minnesota/Twin Cities, Minneapolis, MN 55455, USA
[11] Department of Astronomy and Astrophysics, University of Chicago, Chicago, IL 60637, USA
[12] Department of Astronomy, University of Illinois, 1002 West Green Street, Urbana, IL 61801, USA
[13] Department of Astrophysics and Planetary Science, Villanova University, 800 E. Lancaster Avenue, Villanova, PA 19085, USA
[14] Department of Physics and Astronomy, University of California, Los Angeles, Box 951547, Los Angeles, CA 90095-1547 USA
[15] Center for Interdisciplinary Exploration and Research in Astrophysics (CIERA), and Department of Physics & Astronomy, Northwestern University, 2145 Sheridan Road, Evanston, IL 60208, USA
[16] Max-Planck-Institute for Astronomy, Königstuhl 17, D-69117 Heidelberg, Germany
[17] NASA Headquarters, 300 E Street SW, DC 20546, USA
[18] Department of Astronomy, Cornell University, Ithaca, NY 14853, USA
[19] Johns Hopkins University, Baltimore, Department of Physics & Astronomy, MD 21218, USA
[20] NASA Goddard Space Flight Center, Greenbelt, MD 20771, USA
[21] Harvard-Smithsonian Center for Astrophysics, 60 Garden Street, Cambridge, MA, USA
[22] Department of Physics and ITCP, University of Crete, Voutes, GR-71003 Heraklion, Greece
[23] IESL and Institute of Astrophysics, Foundation for Research and Technology-Hellas, P.O. Box 1527, GR-71110 Heraklion, Greece
[24] USRA/SOFIA, NASA Armstrong Flight Research Center, Building 703, Palmdale, CA 93550, USA
Received 2018 October 26; revised 2018 December 11; accepted 2018 December 16; published 2019 January 4

Abstract

We present far-infrared polarimetry observations of M82 at 53 and 154 μm and NGC 253 at 89 μm, which were taken with High-resolution Airborne Wideband Camera-plus (HAWC+) in polarimetry mode on the Stratospheric Observatory for Infrared Astronomy. The polarization of M82 at 53 μm clearly shows a magnetic field geometry perpendicular to the disk in the hot dust emission. For M82 the polarization at 154 μm shows a combination of field geometry perpendicular to the disk in the nuclear region, but closer to parallel to the disk away from the nucleus. The fractional polarization at 53 μm (154 μm) ranges from 7% (3%) off nucleus to 0.5% (0.3%) near the nucleus. A simple interpretation of the observations of M82 invokes a massive polar outflow, dragging the field along, from a region ~700 pc in diameter that has entrained some of the gas and dust, creating a vertical field geometry seen mostly in the hotter (53 μm) dust emission. This outflow sits within a larger disk with a more typical planar geometry that more strongly contributes to the cooler (154 μm) dust emission. For NGC 253, the polarization at 89 μm is dominated by a planar geometry in the tilted disk, with weak indication of a vertical geometry above and below the plane from the nucleus. The polarization observations of NGC 253 at 53 μm were of a insufficient signal-to-noise ratio for a detailed analysis.

Key words: galaxies: starburst – instrumentation: polarimeters

1. Introduction

Starburst galaxies are an important phenomenon in the universe due to the presence of enhanced star formation and the accompanying strong outflows into the intergalactic medium. This type of galaxy might be an important contributor to the magnetization of the intergalactic medium in the early universe (e.g., Kronberg et al. 1999; Bertone et al. 2006), but the generation and morphology of magnetic fields in starburst galaxies is poorly understood. Galactic scale winds are expected to be important at high redshift where starburst galaxies should be much more common than at the present epoch (e.g., Veilleux et al. 2005). Nearby starburst galaxies

Table 1
Observation Log

Object	λ_c μm	FWHM[a] $''$	Obs. Date Y/M/D	Chop Throw $''$	Chop Angle °, E of N	DP[b]	Obs. Time s
M82	53	5.5	2016 Dec 8	180	cross el.	16	4243
	154	15.3	2017 Oct 24	180	cross el.	8	2141
			2018 Sep 27	180	cross el.	8	2089
NGC 253	53	5.5	2017 Oct 19	300	−40	6	1660
	89	8.8	2017 Oct 19	300	−40	7	2283

Notes.
[a] The tabulated FWHM includes smoothing in the map generation.
[b] Number of dither positions observed, with each consisting of a complete half-wave plate cycle.

with massive outflows provide an excellent laboratory for the study of starburst-driven winds where we can spatially resolve the wind and study the magnetic field geometry in detail. The relationship between spiral arms, outflows, galaxy–galaxy interactions, and the magnetic field geometry has been extensively investigated in the radio (see Beck 2015; Beck & Wielebinski 2013, for a review). Radio synchrotron emission arises from relativistic electrons and may not sample the same volume of gas as interstellar polarization, which is created by extinction or emission from asymmetric dust grains aligned with respect to the ambient magnetic field (e.g., Jones & Whittet 2015).

An early suggestion that galaxies with strong infrared emission may be undergoing intense star formation was made by Harper & Low (1973), based on far-infrared (FIR) observations of M82 and NGC 253. Because it is so well studied, M82 is considered the archtypical starburst galaxy (e.g., Telesco 1988; Telesco et al. 1989) with an infrared luminosity of $3 \times 10^{10} L_{\odot}$ and a star formation rate estimated at $13 M_{\odot}$ yr^{-1}. Based on extensive near-infrared (NIR) integral field spectroscopy, Förster Schreiber et al. (2003) find that M82 is forming very massive stars ($\gtrsim$50–100 $M_{\odot}$). Their analysis suggests that the global starburst activity in M82 occurred in two successive episodes. The first episode took place 10^7 yr ago and was particularly intense at the nucleus, while the second episode occurred 5×10^6 yr ago, predominantly in a circumnuclear ring and along what is believed to be a central stellar bar (e.g., Larkin et al. 1994).

Similar to many galaxies with intense starbursts in their nuclear regions, M82 has a bipolar superwind emanating from the central region, stretching well into the outer halo area (e.g., Shopbell & Bland-Hawthorn 1998; Ohyama et al. 2002; Engelbracht et al. 2006). The geometry of the magnetic field in the central starburst and in the superwind can be investigated using a number of different techniques. Classic interstellar polarization (in extinction) at 1.65 μm in the NIR by Jones (2000) showed evidence for a near-vertical field geometry at the nucleus. However, optical and NIR polarimetry is strongly contaminated by the scattering of light from the very luminous nucleus of M82.

Radio synchrotron observations also trace magnetic fields. Reuter et al. (1994) found that the center of M82 is largely depolarized due to differential Faraday rotation. They find evidence for a vertical field in the northern halo and a more planar geometry in the southwestern disk region. Adebahr et al. (2017) also find a planar geometry in this region and propose a magnetic bar that stretches across the entire central region. They detect some polarization at the nucleus and find that the field is vertical there and can be traced out to 600 pc (35$''$, assuming a distance of 3.6 Mpc; Karachentsev & Kashibadze 2006) into the halo. They conclude that some of the non-detection of polarized emission 200 pc north from the nucleus is most likely caused by canceling of polarization by the superposition of two perpendicular components of the magnetic field along the line of sight.

At a distance of 3.5 Mpc (Rekola et al. 2005), NGC 253 is also a well-studied starburst galaxy with a strong galactic wind (e.g., Sharp & Bland-Hawthorn 2010) and strong mid-infrared (MIR) and FIR emission (Rieke et al. 1980). Unlike M82, which is seen nearly edge-on, NGC 253 has a visible tilt of about 12° (de Vaucouleurs 1958), exposing its nuclear regions and revealing a spiral pattern in the disk. The outflow, projected against the tilted disk, is not as prominent as in M82. However, as in M82, it is seen in several tracers, including emission from dense molecular gas (Bolatto et al. 2013; Walter et al. 2017). Radio observations of NGC 253 do not show evidence for a vertical magnetic field geometry in the nucleus (Heesen et al. 2009). Rather, the polarization map is consistent with a largely planar (disk) geometry.

Polarimetry at FIR wavelengths does not suffer from scattering effects. The albedo is $\gamma < 10^{-5}$ (Draine & Lee 1984). Faraday rotation, which is proportional to λ^2 (Equations (3)–(71); Spitzer 1978), is also insignificant. Also, it traces the column density of dust, which is much more closely tied with the total gas column density than the relativistic electrons producing the radio synchrotron emission. While the FIR-radio emission correlation (Helou et al. 1985) might suggest that the energy in cosmic-ray electrons and the thermal dust emission are strongly associated, it is not clear that they trace the same magnetic field geometry. With the advent of an FIR polarimetric imaging capability on the Stratospheric Observatory For Infrared Astronomy (SOFIA) via the High-resolution Airborne Wideband Camera-plus (HAWC+; Harper et al. 2018), we can now map the magnetic field geometry in both the disk and central regions of M82 and NGC 253 with the goal of understanding the role of magnetic fields in starburst galaxies.

2. Far-infrared Polarimetric Observations

M82 and NGC 253 were observed as part of the Guaranteed Time Observation program with HAWC+ (Vaillancourt et al. 2007; Dowell et al. 2010; Harper et al. 2018) on the 2.5 m SOFIA telescope. We made observations of the inner regions of these galaxies using the standard chop-nod polarimetry mode with the instrumental configurations shown in Table 1. HAWC+ polarimetric observations simultaneously measure two orthogonal components of linear polarization using a pair

of detector arrays with 32 columns × 40 rows each. Observations were acquired with a sequence of four dither positions in a square pattern with a half side length of three pixels. Integrations with four half-wave plate angles were taken at each dither position. Based on the morphology of the sources evident in *Herschel* maps (Roussel et al. 2010; Pérez-Beaupuits et al. 2018), the chop throw and angle are sufficient to make the intensity in the chop reference beams negligible for the results reported here.

Data were reduced using the HAWC+ Data Reduction Pipeline v1.3.0beta3 (2018 April), but with some customizations to address these particular data sets. The data for all dither positions were screened for quality in the telescope tracking and basic instrument function, resulting in exclusion of one dither position for NGC 253 at 89 μm. As is standard with v1.3.0beta3, a χ^2 test was performed by intercomparing dither sets. We found that the statistical uncertainties were underestimated by a small, typical amount, and we inflated the uncertainties to account for this. The inflation factors ranged from 1.19 to 1.34 for Stokes Q and U.

For subtraction of instrumental polarization, we used a revised calibration data product (v2, 2018 August); this is based on "polarization skydips" as is the previous standard calibration product and differs by only Δq or $\Delta u \approx 0.1\%$ from it, but it is believed to be more accurate.

Close inspection of the M82 154 μm data revealed a likely crosstalk effect in the detector system, in which a bright source produces a small, artificial response in another detector in the same readout column. The magnitude of this effect is approximately 0.01%–0.1% of the signal in the detector with the bright source, and it seems to affect a fraction of the rows that are read out following the bright source. This crosstalk was confirmed in separate observations of planets, and it may be similar to a crosstalk effect observed in certain calibration data from BICEP2 (Brevik 2012), which has some cryogenic and room-temperature detector readout circuit designs in common with HAWC+. We have not yet been able to develop a detailed model for the crosstalk, including its apparent variability over time; instead, we identify measurements (with granularity of "dither position" and "detector pair") that are likely to be affected significantly by the crosstalk and discard them.

Specifically, we looked at positions away from the bright cores of the galaxies for inconsistency in the "$R + T$" total intensity signal among the eight nods comprising the fundamental polarization measurement sequence (a single dither position with four half-wave plate angles). The $R + T$ detector pair sum (Harper et al. 2018) should be constant over the eight nods (independent of polarization) except for noise, calibration drifts, and artifacts in the detector system.

For the M82 154 μm data, most of the suspect measurements identified and removed were found in the same column as bright galaxy emission and in rows that are read out afterward, indicative of the crosstalk effect. For the other data sets, we found fewer inconsistent $R + T$ measurements, and the majority of them correspond to otherwise noisy detectors. We removed 0.03%–0.7% of the measurements with this first cut, depending on the observation. We followed this with a general-purpose deglitcher, which operates in the map domain, as described by Chuss et al. (2018). Approximately 0.1%–0.7% of measurements were removed by the deglitcher. For the two epochs of the M82 154 μm observations, the parallactic angle differed by ∼80°, which improved the deglitching performance and map uniformity.

Table 2
Integrated Properties

Map	Radius (″)	I (Jy)	P (%)	PA (E, °)
M82 53 μm	45	2110	1.5	81
M82 154 μm	60	1430	0.1	···
NGC 253 53 μm	15	960	0.1	···
NGC 253 89 μm	30	1450	0.4	160

For M82 at both wavelengths and NGC 253 at 89 μm, spatially extended polarization was detected with statistical significance in excess of 10σ in parts of each map. Our 53 μm observation of NGC 253 has significantly lower signal-to-noise (S/N) in polarization, however, and since the effective integration time across the galaxy nucleus varies significantly due to the source falling on inoperational detectors for several of the dither positions, the polarization map is difficult to interpret. For this observation, we report only an integrated signal in Table 2.

3. M82: Dust Temperature and Column Density

Previous lower spatial resolution M82 observations at FIR wavelengths by Kaneda et al. (2010) find a dust mass of $2.3 \times 10^6\,M_\odot$ within the central 2′ using a multiple-dust temperature fit to their *AKARI* data. Using a gas-to-dust ratio of 100, this corresponds to a total mass (gas and dust) of $M_{\rm tot} \sim 2 \times 10^8\,M_\odot$. By subtracting the FIR emission from the starburst and the disk of M82, Roussel et al. (2010) estimate the total dust mass in the wind and halo from their 500 μm and dust temperature maps to be $(1.1 \pm 0.5) \times 10^6\,M_\odot$, or $M_{\rm tot} \sim 1 \times 10^8\,M_\odot$. Using FORCAST on SOFIA, Nikola et al. (2012) were able to image the inner 75″ of M82 at wavelengths from 6.6 to 37.1 μm at an angular resolution of ∼4″ (70 pc). Their analysis uses measurements of extinction and surface brightness to constrain the total mass and dust mass of the two central peaks seen at NIR and MIR wavelengths. They find $A_V = 18$ and $A_V = 9$ toward the main and secondary emission peaks with an estimated color temperature of 68 K at both peaks. The dust masses at the peaks within a $6\farcs6 \times 6\farcs6$ region were estimated to be $\sim 10^4\,M_\odot$, or $M_{\rm tot} \sim 10^6\,M_\odot$. Based on the M82 rotation curve (Greco et al. 2012), the total mass within a 100 pc (5.″7) radius of the center is $M_{100} \sim 5 \times 10^7 M_\odot$ and within a 500 pc (28.″6) radius, $M_{500} \sim 1.5 \times 10^9 M_\odot$.

To support the polarimetric analysis, we made temperature and column density maps of M82. Specifically, we combine our 53 and 154 μm HAWC+ observations with the publicly available 70, 160, and 250 μm observations from the *Herschel Space Observatory* (Pilbratt et al. 2010) with the PACS instrument (Poglitsch et al. 2010) and SPIRE instrument (Griffin et al. 2010). These observations were taken as part of the Very Nearby Galaxies Survey (PI: Christine Wilson). We bin each observation to the pixel scale, 6″, of the 250 μm *Herschel* image. We then extract the intensity values of each pixel associated to the same part of the sky at each wavelength. Finally, we fit a modified blackbody function assuming a dust emissivity of $\epsilon_\lambda \propto \lambda^{-1.6}$ (e.g., Boselli et al. 2012), with the temperature and optical depth at 250 μm, τ_{250}, left as free

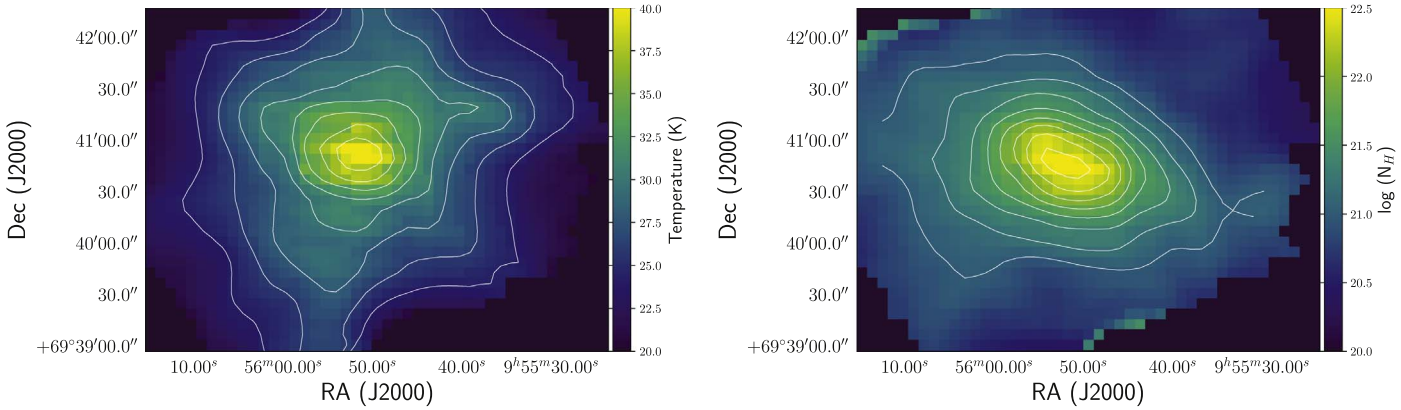

Figure 1. M82 maps of color temperature (left) and column density (right). The temperature contours start at 20 K and increase in 2 K increments. The column density contours start at $\log(N(\mathrm{H} + \mathrm{H_2})) = 21$ and increase in increments of 0.2.

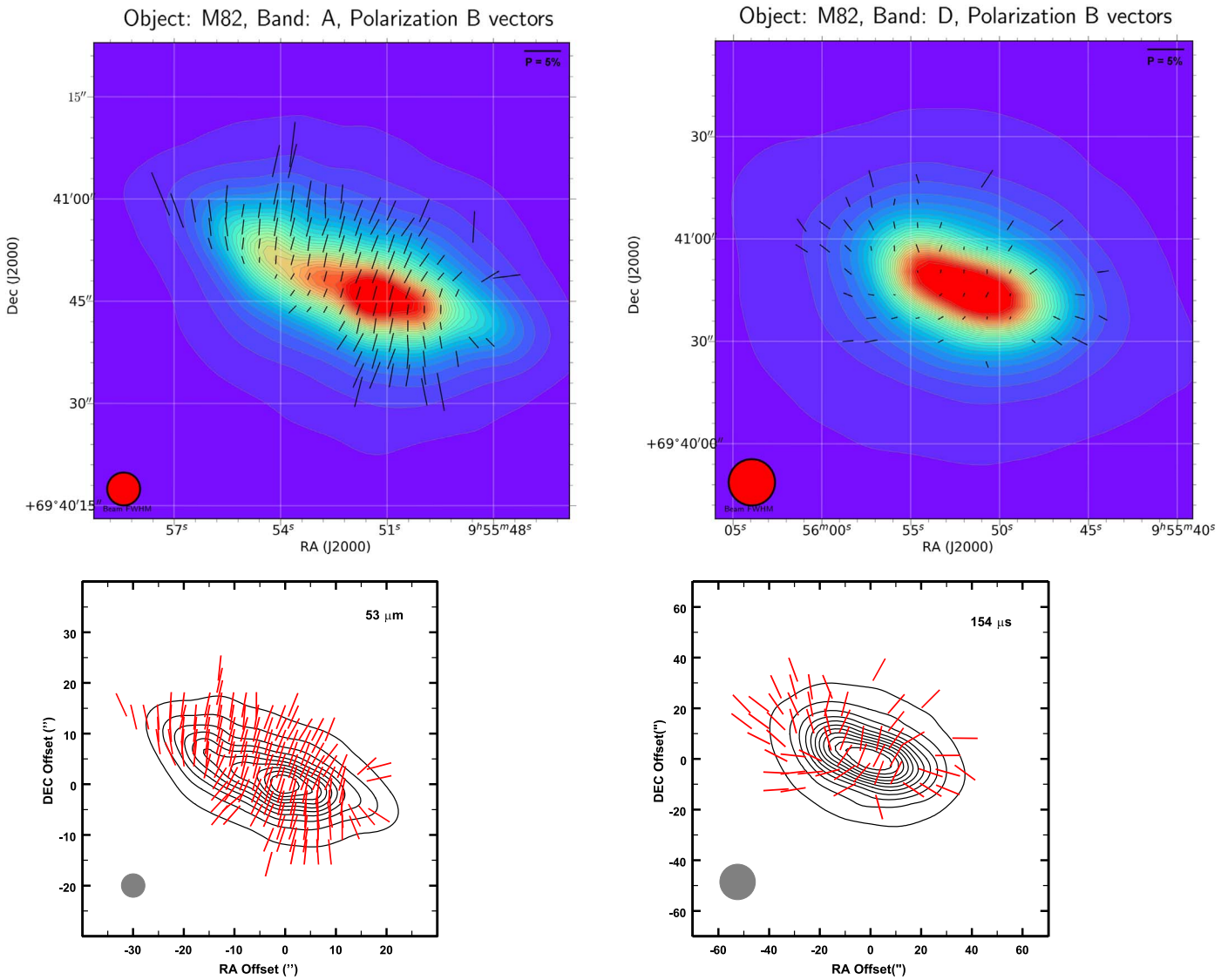

Figure 2. Polarization vector maps of M82, rotated 90° to represent the inferred magnetic field direction. Upper left: 53 μm fractional polarization. Upper right: 154 μm fractional polarization. Bottom left: position angle only overlaying intensity contours. The first contour starts at 2×10^4 MJy sr^{-1} with increments of 2×10^4 MJy sr^{-1}. Bottom right: position angle only overlaying intensity contours. The first contour starts at 4×10^3 MJy sr^{-1} with increments of 4×10^3 MJy sr^{-1}.

parameters. We compute $N(\mathrm{H} + \mathrm{H_2}) = \tau_{250}/(k\mu \mathrm{m_H})$, where $k = 0.1\,\mathrm{cm^2\,g^{-1}}$ (Hildebrand 1983) and $\mu = 2.8$. We use the HAWC+ data to both augment the *Herschel* data and help constrain the Wien side of the spectral energy distribution (SED) at 53 μm. Figure 1 shows both the temperature and column density maps within the same field of view (FOV).

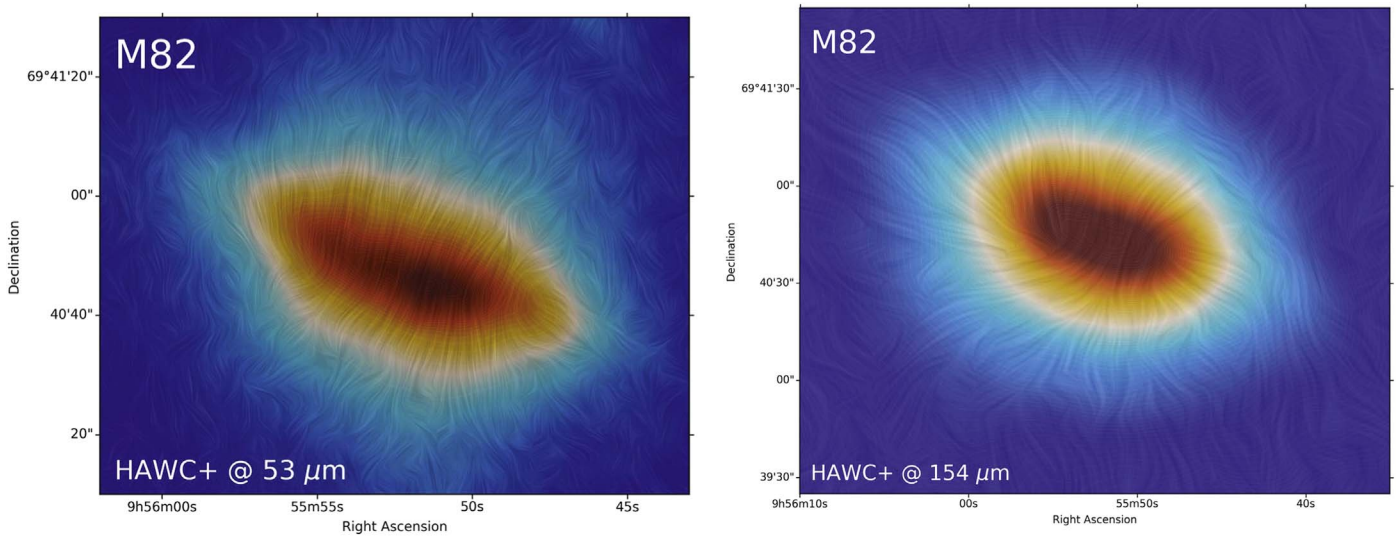

Figure 3. Line integral contour (Cabral & Leedom 1993) maps of the polarization data. Notice the transition of the position angle from vertical to planar to the southwest in the 53 μm map and to both the northeast and southeast in the 154 μm map. A cut in polarization S/N (debiased) of 2σ was used to form these images, which allows the general trend in position angle to be traced further into the halo and along the disk.

The color temperature ranges from a peak of 40 K on the nucleus to 25 K at about 20″ along the disk to the northeast and southwest. The computed column density peaks at $N(\mathrm{H} + \mathrm{H}_2) = 3 \times 10^{22}$ cm^{-2}, about $A_V \sim 20$, somewhat higher than that found by Nikola et al. (2012). Summing the column density in a 40″ × 20″ box yields $M_{\rm tot} \sim 8 \times 10^7\, M_\odot$. This is at least a factor of two less than what is seen in the molecular gas in the same region. Given the filling factor of 1% for the dense gas derived by Naylor et al. (2010), most of the molecular gas, even if the temperature of the dust on the surface of the dense cores was as high as 50 K, is probably not contributing significant flux to our HAWC+ maps. This means our HAWC+ observations do not sample regions of very dense, molecular cores, but rather, they sample the dust associated with the rest of the interstellar matter (ISM) in M82, including less dense ($\rho \lesssim 100$ cm^{-3}) molecular gas.

4. M82: Polarization Maps

The SOFIA observations of M82 are shown in Figure 2, where we have plotted polarization vectors on a grid with one-half beamwidth for the spacing and with position angles rotated 90° to represent the inferred magnetic field direction. In the top row, the vector length is proportional to the fractional polarization. Cuts for the fractional polarization were made at an S/N of 3.3/1 (debiased; see Wardle & Kronberg 1974) and at an intensity of 0.21 Jy/□″ at 53 μm and 0.044 Jy/□″ at 154 μm. Since HAWC+ is a relatively new instrument, we chose to be conservative in our S/N cuts. Also, since there is a large number of pixels outside these intensity contours (∼1000), we used the cut in intensity to remove a few statistically insignificant pixels with no corroborating nearby position angles. We can likely trust the remaining vectors as being indicative of the field direction. In the second row, all vectors within these criteria are plotted with the same length to better clarify the position angle morphology. At a wavelength of 53 μm, the polarization fraction ranges from a high of 7% well off the nucleus to values as low as 0.5% at some locations along the plane (disk) of M82. The fractional polarization at the intensity peak is 2.2%, and it declines toward the east and west along the plane. Although the nominal systematic error in polarization for HAWC+ is 0.3% (1σ; Harper et al. 2018), in this specific map, detections with p as low as 0.5% appear to have position angles that fit the large-scale pattern. Line integral contour maps using lower S/N data are shown in Figure 3 to better illustrate the mean position angle at greater distances from the disk.

Clearly evident in the 53 μm image is the presence of a magnetic field geometry largely perpendicular to the plane. This geometry extends over a region at least 700 pc (40″) along the disk and up to 350 pc above and below the plane. The stellar scale height for the thin disk in M82 is $h_z = 143$ pc (Lim et al. 2013), however the more extended distribution of asymptotic giant branch (AGB) stars is much greater (Davidge 2008). We do not measure the magnetic field geometry in the outflow at kiloparsec scales.

For the polarization map at 154 μm, the polarization fraction ranges from a high of 3% well off the nucleus to 0.3% near the nucleus, and the vectors show more variation than in the 53 μm map. The polarization vectors in the central region and to the north and northwest are consistent with a vertical field. The vertical field is displayed by vectors with fractional polarization ranging from 4% in the northwest to only 0.3% in the disk, so some caution is needed in interpreting the detailed field structure. The vectors to the southwest and northeast along the disk have larger magnitude (most >1%) and indicate a geometry closer to parallel to the plane of the disk. Using NIR polarimetry in extinction, Jones (2000) found evidence for a vertical geometry at the nucleus, but a planar geometry to the southwest of the central region. Our FIR observations agree with the geometry found by Jones (2000), but the NIR observations were heavily contaminated by scattering polarization and were not conclusive. Our 154 μm polarimetry is consistent with a planar disk geometry for the magnetic field visible in the polarization vectors to either side of the nuclear starburst. There is evidence for this in the 53 μm map as well in a few vectors to the southwest and perhaps the northeast.

Using the SCUBA camera on the James Clerk Maxwell telescope, Greaves et al. (2000) reported an 850 μm polarization map for M82 consisting of 22 polarization vectors

with $>3\sigma$ significance and covering a $40'' \times 50''$ region similar to ours. The main features of the map are a vertical magnetic field at the west nucleus, (inferred) low polarization at the east nucleus, and a loop or bubble shape to the field at the outskirts of the map. Matthews et al. (2009) reprocessed the 850 μm data as part of an archive paper and produced a map with 16 vectors at $>2\sigma$ significance. The vertical field at the west nucleus is still apparent, as is the (inferred) low polarization at the east nucleus, but the loop is no longer clear. The dust emitting at 850 μm should also contribute significantly in the HAWC+ 154 μm band. Comparing the maps at those two wavelengths, we find agreement regarding the vertical magnetic field toward the west nucleus and the decrease in fractional polarization toward the east. However, we do not observe the loop field, nor do we see other clear similarities. We performed a statistical test of agreement between each version of the 850 μm map and our 154 μm map. For each reported 850 μm vector, we interpolated the 154 μm Stokes parameters (Q_{154}, U_{154}) and formed the dot-product-like quantity of $S = Q_{154}Q_{850} + U_{154}U_{850}$. Positive values of S indicate an agreement of polarization angles within 45°, and negative values indicate a disagreement greater than 45°. We observe a positive correlation for the 2–3 850 μm measurements toward the west nucleus, but for the remaining 13–20 measurements we find just as many positive as negative values of S. Of all the FIR/submillimeter polarization maps discussed in this section, the HAWC+ 53 and 154 μm maps are the only ones that clearly show a correlation over an extended area.

Jones (2000), observing polarization in extinction at 1.65 μm, interpreted the combination of a vertical position angle in the nucleus and a planar geometry in the disk as a mixture of two magnetic field geometries along the line of sight. The field in the central regions with the starburst is vertical, while the field in the surrounding disk is planar. In extinction, this causes a partial cancellation of the fractional polarization as the light from the nucleus first traverses the region with a vertical field and then traverses the disk with a planar magnetic field. In essence, the two regions act as crossed polaroids (more accurately crossed fields). Based on the expected level of fractional polarization for the measured extinction to the nucleus of M82 in the NIR (Jones 1989, 1993), Jones (2000) estimated that two-thirds of the dust along the line of sight to the nucleus has a vertical field, with the remainder of the dust lying in the disk passing in front of the nucleus.

The polarization in extinction is a function of the column depth of dust along the line of sight, but not the dust temperature. In emission at FIR wavelengths, hotter dust will radiate more effectively at shorter wavelengths than cooler dust. Referring to our dust temperature map, the 53 μm emission is more sensitive to temperature than the 154 μm emission because it is on the Wien side of the SED. Hence, the 53 μm emission can dominate over the 154 μm emission for regions along a path with warmer dust. Since the dust in the central region is hotter than in the disk (see Figure 1), the transition from a vertical to a planar position angle will take place more quickly at 154 μm than at 53 μm as the line of sight moves away from the nucleus along the disk. This is what we observe. If the dust temperature were constant everywhere in the disk, then the transition of the magnetic field geometry from planar to vertical would presumably take place at the same location for both wavelengths.

The vertical magnetic field geometry we see in the HAWC+ FIR polarimetry lies along the same direction seen in other measurements of the supergalactic wind in M82. Optical and Hα images suggest a conical outflow with a fairly narrow launch point in the nucleus. Line splitting seen in CO observations of the molecular gas is interpreted as due to a conical outflow perpendicular to the disk with an opening angle of 20° that stretches up to 1.5 kpc from the nucleus (Walter et al. 2002). Martini et al. (2018) show that the HI kinematics are inconsistent with a simple conical outflow centered on the nucleus, but instead require the more widespread launch of the HI over the ~1 kpc extent of the starburst region. This result is consistent with our finding that the region in the disk with a vertical magnetic field is at least 700 pc wide. There is some evidence that the polarization vectors in the 154 μm map to the east line up with streamers S2, S4, and possibly S3 seen in the CO observations of Walter et al. (2002).

5. M82: The Threaded Field

The magnetic field in the ISM of spiral galaxies has both constant (threaded) and turbulent components (see a recent treatment by Planck Collaboration et al. 2018). The effects of a turbulent component can be seen in both variations of the polarization position angle with position on the sky using a type of structure function (Kobulnicky et al. 1994; Hildebrand et al. 2009; Planck Collaboration et al. 2018) and the trend of fractional polarization with column depth (e.g., Hildebrand et al. 1999; Jones et al. 2015). We will examine the structure function in a later paper, but we can easily examine the trend of fractional polarization with optical depth. If the magnetic field geometry is perfectly constant with no bends or wiggles, the fractional polarization in emission will be constant (see Jones et al. 2015; Jones & Whittet 2015, for a review) with optical depth in the optically thin regime. If there is a region along the line of sight that has completely unaligned grains, it will add total intensity to the beam, but no polarized intensity, resulting in a slope of $P \propto \tau^{-1}$ with increasing contribution from that region (Jones et al. 2015).

If the dust grain alignment angle varies in a purely stochastic way along a line of sight, the fractional polarization in emission will decrease as $P \propto \tau^{-1/2}$ (Jones et al. 2015), and there will be no correlation in position angle across the sky. A combination of a constant and a purely random component will cause the polarization to decrease with optical depth at a rate in between these two extremes, with the constant component dominating the position angle geometry after several decorrelation lengths (Zweibel 1996). If there is a coherent departure from a purely constant component such as a spiral twist, paths with perpendicular magnetic fields, or other smooth variations of the projected field along the line of sight that depend on total column depth, the fractional polarization can drop faster than $P \propto \tau^{-1/2}$ due to strong cancellation of the polarization. Note, in this context, we are considering the field in the outflow of M82 to have a threaded component aligned with the outflow.

We are assuming the efficiency of the grain alignment mechanism is not a factor in our FIR polarimetry of M82 (see Andersson et al. 2015, for a review of grain alignment). We argued in Section 3 that our observations are sensitive to the warm dust in the diffuse ISM of M82, but are largely insensitive to contributions from very dense molecular cloud cores. There is good evidence that grain alignment in the Milky Way is at its maximum in the diffuse ISM, and only in dense

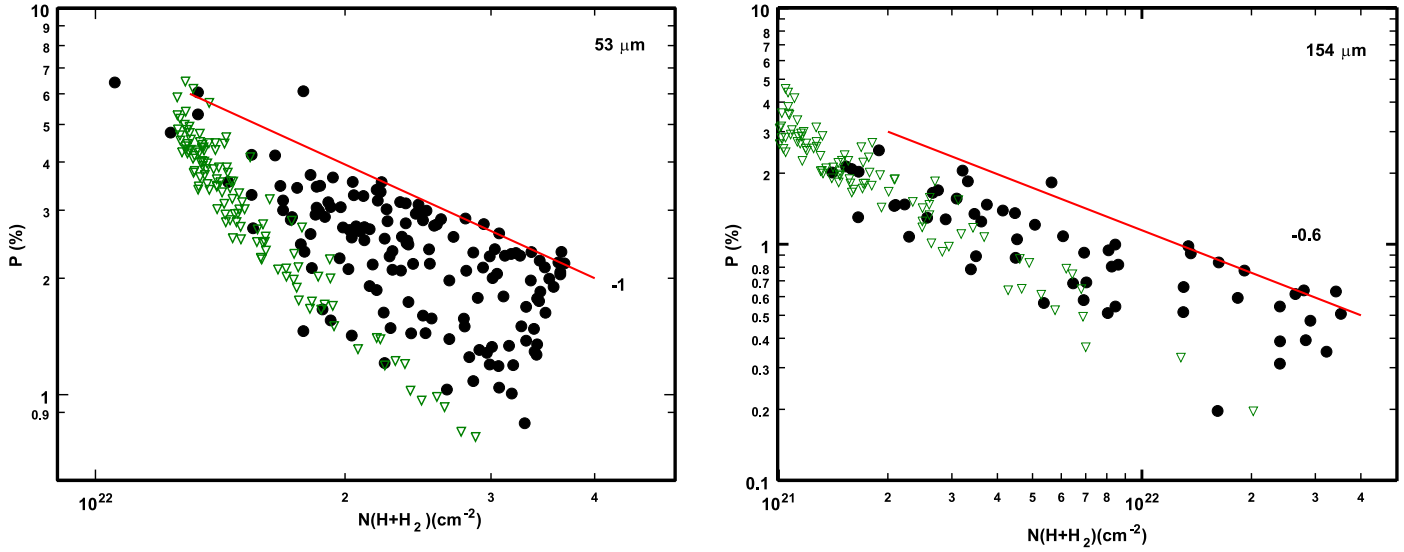

Figure 4. Plot of fractional polarization against $N(\mathrm{H} + \mathrm{H_2})$ column depth for high S/N data points at 53 and 154 μm for M82. The 3.3σ upper limits are plotted as green triangles.

cloud cores with no internal radiation field is there a possible loss of grain alignment (Jones et al. 2015). Since our HAWC+ observations are not sensitive to very dense molecular cloud cores, we do not expect regions with unaligned grains to contribute to our FIR polarimetry. We cannot rule out that regions of very high turbulence (scrambled field) on small scales may be present along some lines of sight, mimicking regions with unaligned grains (adding net total intensity, but no net polarized intensity).

Figure 4 plots the trend in fractional polarization with column density at 53 and 154 μm. The 3.3σ upper limits are plotted as green triangles. Simple power-law fits to the upper bound of the data points in Figure 4 are steeper than $P \propto \tau^{-1/2}$ at 53 μm and about the same at 154 μm. We are concentrating on the upper bound in these plots because that delineates lines of sight where the minimum depolarization effects are present. Lines of sight with lower P could suffer significant depolarization effects, but it is hard to point to a specific line of sight and conclude which effects are dominant. If a crossed field effect is at work along lines of sight through the plane of the disk, and it spans most of the area we have mapped, then it will lower the overall fractional polarization. Although the slope of P versus $N(\mathrm{H} + \mathrm{H_2})$ at 53 μm is about $P \propto \tau^{-1}$, the clear coherence of the position angles across the face of M82 indicates that a systematic cancellation of polarization is most likely taking place.

The fraction of the gas with a vertical field is difficult to determine. If the very low fractional polarization in the nucleus is due to simple cancellation of polarization by the superposition of a planar disk field and a polar nuclear field, then (using the value of two-thirds for the column depth corresponding to the vertical component in Jones 2000) approximately (5–6) $\times$ $10^7\,M_\odot$ has entrained a vertical field. If, however, turbulence on a small scale relative to our beam dominates the field geometry in the warm dust, leaving only a modest fraction of the dust with a coherent polar field, then this must be considered as an upper limit. If the estimates of the molecular gas mass in M82 are correct (see Section 3), then a significant fraction of the mass in the nuclear region of M82 is not detected by our FIR polarimetry.

6. NGC 253

In this section, we present the 89 μm results of NGC 253, and these observations have an interesting contrast to those of M82.

The SOFIA/HAWC+ 89 μm observations of NGC 253 are shown in Figure 5, where we have plotted polarization vectors on a grid with half beam-width for the spacing and with position angles rotated 90° to represent the inferred magnetic field direction. M82 ($d = 3.6$ Mpc) and NGC 253 ($d = 3.5$ Mpc) are at very similar distances, so our maps in RA and delc. are on nearly the same physical scale. On the left, the vector length is proportional to the fractional polarization. On the right, all of the vectors are plotted with the same length to better clarify the position angle morphology. Cuts in fractional polarization are at the same S/N (3.3/1 debiased) as for M82, but with a cut at a intensity contour of 0.38 Jy/□″ at a wavelength of 89 μm. The polarization fraction ranges from a high of 2% well off the nucleus to 0.1%–0.2% on the nucleus. The polarization at the nucleus is below our nominal systematic error of 0.3%, but the position angle is consistent with the vectors to the northeast and southwest along the major axis, not a vertical geometry. Unlike M82, the rotated polarization vectors lie largely along the long axis of the tilted disk in NGC 253. However, there is some evidence for a vertical field geometry above and below the plane to the northwest and southeast along the minor axis.

Radio synchrotron observations of NGC 253 (Heesen et al. 2009) show a magnetic field geometry that consists of disk and halo components. The disk component dominates the visible disk with the magnetic field orientation parallel to the disk at small distances from the midplane. Well out in the halo, the field (as measured at radio wavelengths) shows the familiar X-shape seen in several nearly edge-on galaxies (Beck & Wielebinski 2013). The radio observations show no indication of a vertical component along the minor axis of the tilted disk. We do find several vectors away from the plane (dotted line in Figure 5) that might be indicative of a vertical component, but such a vertical field is much more obvious in M82. Compared to M82, NGC 253 cannot have as large of a fraction of the dust column depth containing a vertical field.

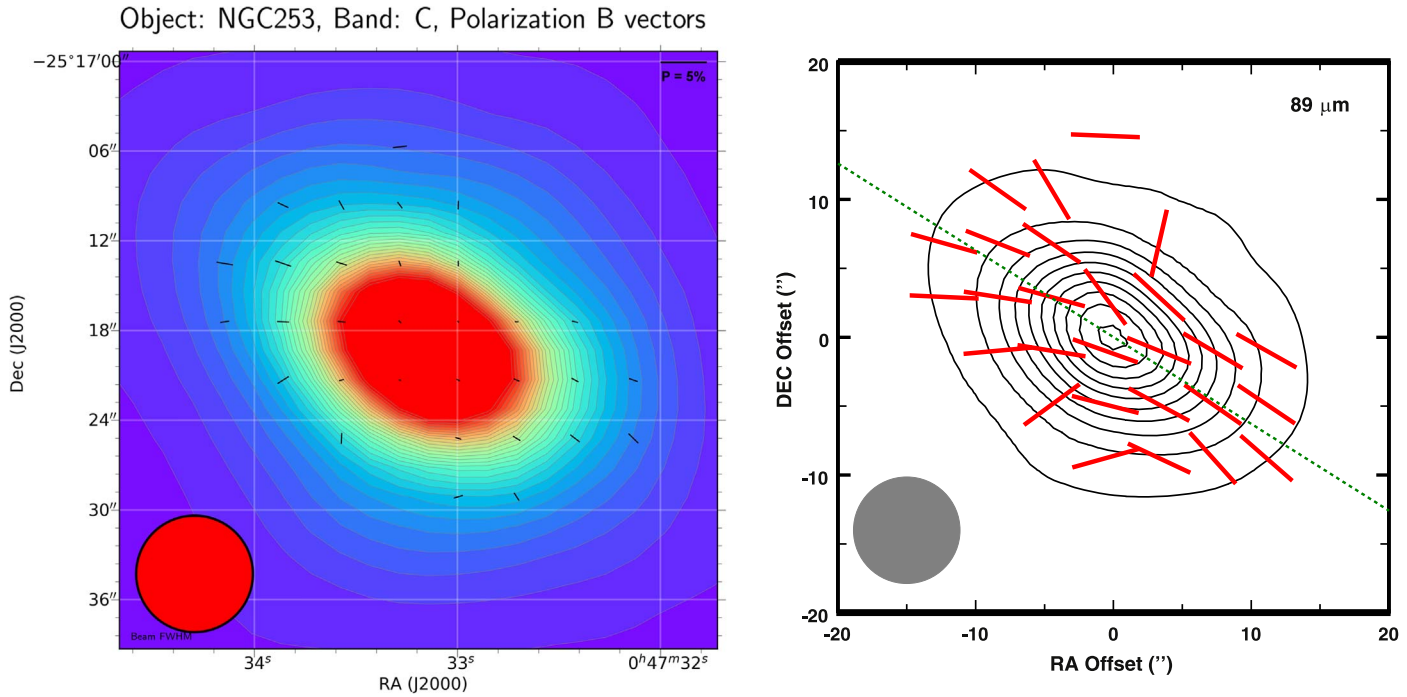

Figure 5. Polarization vector map of NGC 253 at 89 μm, with vectors rotated 90° to represent the inferred magnetic field direction. Left: vectors with length proportional to the fractional polarization. Right: position angle only, overlaying intensity contours. The first contour starts at 2.8×10^4 MJy sr^{-1} with increments of 2.8×10^4 MJy sr^{-1}. The dashed line indicates the long axis of the tilted disk (position angle = 51°, Pence 1980).

Figure 6 plots the trend of fractional polarization with surface brightness, similar to Figure 4 for M82, except we are using surface brightness as a proxy for optical depth. The upper limits are plotted as green triangles. The data show a decline in polarization with intensity, similar to M82. A rough fit to the slope of this trend is much steeper than $P \propto I^{-1/2}$. The steeper decline in polarization with intensity seen in NGC 253 must be due to greater large-scale cancellation effects with column depth in this galaxy. As with M82, if a crossed field effect is at work, and it spans most of the area we have mapped, then it will lower the overall fractional polarization. Since none of the vectors near the nucleus along the disk show a vertical geometry, any crossed field effect taking place must be dominated by the polarization in the disk, not the wind. For M82 we were able to use the NIR polarimetry to roughly estimate the fraction of the column depth that had vertical and planar fields. We do not have NIR polarimetry of NGC 253, but by analogy, the low net polarization in the disk of NGC 253 would indicate that roughly two-thirds of the column depth contains a planar field, with no more than one-third associated with a vertical field and the supergalactic wind in this galaxy.

7. Discussion: Integrated Properties

The underlying mechanism for producing massive winds from the central regions of starburst galaxies is not understood. Detection of the wind of M82 inspired the pioneering work of Chevalier & Clegg (1985) on thermally driven winds. Later works explored the role of radiation pressure (e.g., Murray et al. 2011; Krumholz et al. 2018), cosmic ray driving (e.g., Everett et al. 2008), and combinations of these effects (Hopkins et al. 2012; Ruszkowski et al. 2017). Thermal models show a tight correlation between central temperature and asymptotic velocity, at least when the wind is sufficiently hot and/or tenuous that radiative cooling is insignificant (Bustard et al. 2017). Thus, $\sim 10^8$ K gas is required to reach the speeds of up to 2200 km s^{-1} detected in the X-ray emitting gas in the wind of M82 (Strickland & Heckman 2007). The origin of the cooler and slower gas observed in the outflow is unclear, although it may form in situ through shock compression in the flow or through the effects of repeated supernova explosions driving supershells in the central regions of molecular disks (Fujita et al. 2009).

It is expected that a wind, whatever its origin, as massive as the one in M82 will drag the magnetic field lines out along with it. In this sense, the transition to a near vertically oriented field in the starburst core of M82 is not surprising. However, given that both the spectroscopic and imaging evidence for the wind is in warm to hot ionized gas, it is notable that the field is vertical in the warm dust, which presumably is situated in mostly molecular gas associated with star-forming regions (but not dense cores). This suggests that the clouds and the intercloud medium are magnetically connected and that the field in the clouds is not overwhelmingly tangled by turbulence. Walter et al. (2002) find kinematic signatures of an outflow in observations of the molecular gas in M82, a characteristic in common with NGC 253 (Bolatto et al. 2013). It is interesting that the observations reported in this Letter show weaker evidence for a vertical field in NGC 253, however.

Polarized emission from aligned dust grains provides information on the magnetic field geometry in the interstellar medium but does not directly measure magnetic field strength, and primarily traces the field in both the diffuse and molecular gas. Indirect methods of measuring field strength such as the Chandraskhar–Fermi method (Chandrasekhar & Fermi 1953) or measures of the dispersion in the position angle (see Houde et al. 2016, and references therein), cannot be applied here as there is simply too much averaging taking place in our 90 pc beam. M82 is a strong emitter of both nonthermal radio

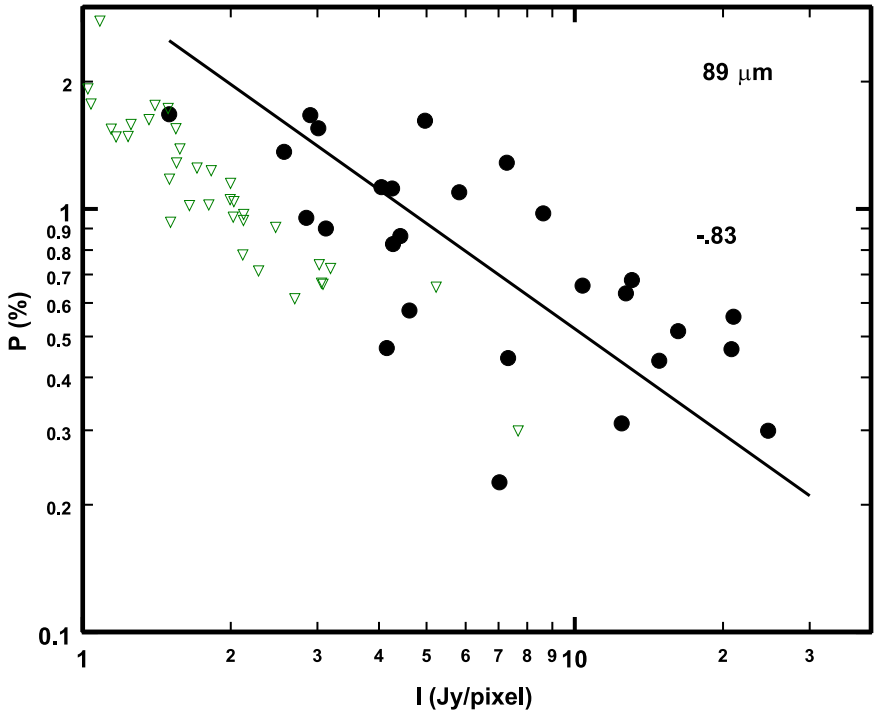

Figure 6. Plot of fractional polarization against surface brightness for high S/N data points at 89 μm for NGC 253. The intensity is being used as a proxy for optical depth. 3.3σ upper limits are shown as green triangles.

radiation and γ-rays, and modeling their spectra can provide an estimate of the mean magnetic field strength (Yoast-Hull et al. 2013). Their best-fit model assumes a total molecular gas mass of $\sim 4 \times 10^8 M_\odot$, a factor of 10 larger than the mass estimated here, to be threaded by the vertical field, and yields $B \sim 250$ μG and a wind speed of 500 km s^{-1}. Their derived magnetic field strength is somewhat above the field strength of 150 μG used by de Cea del Pozo et al. (2009) under the assumption that the magnetic field energy density is in equipartition with the cosmic-ray energy density. A range of models with larger fields and faster winds or smaller fields and slower winds fits the data nearly as well. The field strength is weighted by ISM properties in a complex way, with most of the synchrotron radiation being emitted in the low-density, large filling-factor medium, but most of the γ-rays and secondary leptons are produced in the high density clouds. A similar modeling attempt for NGC 253 (Yoast-Hull et al. 2014) failed to produce a good joint fit for both the radio and γ-ray spectra. Whether the different outcomes for M82 and NGC 253 are related in any way to the different polarization properties reported here is beyond the scope of this Letter.

The Galactic center of the Milky Way also has a vertical magnetic field geometry immediately above and below the inner disk (which itself has a planar field) as evidenced by the presence of numerous magnetized vertical filaments (Yusef-Zadeh et al. 2004; Morris 2006). If the magnetic field strength in these filaments is at the upper end of the range allowed by measurements, $\sim$1 mG, stronger than model estimates for the wind in M82, then the vertical field dominates gas dynamics. Perhaps the vertical field in the Galactic center could have an origin unrelated to winds, unlike our interpretation of the field geometry in M82. Note that if placed at the distance of M82, FIR polarimetry of the Galactic center would likely be dominated by emission from dense molecular clouds with a planar field geometry (e.g., Figure 1 in Chuss et al. 2005).

M82 and NGC 253 are nearby galaxies that allow us to map polarized dust emission on 80–100 pc scales. For comparison with future observations of more distant galaxies, we have computed the integrated properties of these two galaxies in much larger beams. The results are shown in Table 2. Note that the net position angles from the integrated I, Q, and U maps for M82 at 53 μm and NGC 253 at 89 μm preserve information on the magnetic field geometry relative to the disk and wind position angles. This implies that future observations of at least some more distant, unresolved (at FIR wavelengths) galaxies with known jet, wind, or disk geometries can still provide relevant information on the global magnetic field geometry. However, the large-scale planar and vertical components in the 154 μm map of M82 cancel and produce very low fractional polarization in the integrated signal.

8. Conclusions

We have presented FIR polarimetric imaging observations of M82 and NGC 253 using HAWC+ on SOFIA. Effects such as scattering seen at NIR wavelengths and Faraday rotation at radio frequencies are absent in the FIR polarimetry. Unlike radio synchrotron emission, the FIR emission is sensitive to the dust column density (weighted by temperature) along the line of sight, not the population of relativistic electrons. These observations of M82 are consistent with a vertical magnetic field in the central $40'' \times 20''$ region where the starburst is located and a planar magnetic field in the surrounding disk. The fractional polarization is very low at the nucleus, but shows the same vertical field geometry. The low polarization could be due to the mutually perpendicular nuclear and disk fields partially canceling the polarization or this effect in combination with strong turbulence on scales much smaller than our beam. If the

crossed field effect dominates, then $\sim(5–6) \times 10^7\,M_\odot$ in the central region of M82 is threaded with a magnetic field perpendicular to the disk. For NGC 253 the observations at 89 μm are consistent with a planar magnetic field geometry both in nucleus and to the northeast and southwest along the disk. There is some indication of a more vertical geometry along the minor axis, but off the nucleus. Compared to M82, NGC 253 cannot have as much of the dust column depth containing a vertical field.

Based [in part] on observations made with the NASA/DLR Stratospheric Observatory for Infrared Astronomy (SOFIA). SOFIA is jointly operated by the Universities Space Research Association, Inc. (USRA), under NASA contract NAS2-97001, and the Deutsches SOFIA Institut (DSI) under DLR contract 50 OK 0901 to the University of Stuttgart. Part of this research was carried out at the Jet Propulsion Laboratory, California Institute of Technology, under a contract with the National Aeronautics and Space Administration. The LIC code was ported from publicly available IDL source by Diego Falceta-Gonçalves.

Herschel is an ESA space observatory with science instruments provided by European-led Principal Investigator consortia and with important participation from NASA.

Facility: SOFIA.

ORCID iDs

Terry Jay Jones https://orcid.org/0000-0002-8716-6980
Ellen G. Zweibel https://orcid.org/0000-0003-4821-713X
Paul F. Goldsmith https://orcid.org/0000-0002-6622-8396
Ryan T. Hamilton https://orcid.org/0000-0001-6350-2209
Shaul Hanany https://orcid.org/0000-0002-8702-6291
Leslie W. Looney https://orcid.org/0000-0002-4540-6587
Joseph M. Michail https://orcid.org/0000-0003-3503-3446
Mark R. Morris https://orcid.org/0000-0002-6753-2066
Giles Novak https://orcid.org/0000-0003-1288-2656
Fabio P. Santos https://orcid.org/0000-0002-9650-3619
Kartik Sheth https://orcid.org/0000-0002-5496-4118
Johannes Staguhn https://orcid.org/0000-0002-8437-0433
Ian W. Stephens https://orcid.org/0000-0003-3017-4418
Konstantinos Tassis https://orcid.org/0000-0002-8831-2038
Edward J. Wollack https://orcid.org/0000-0002-7567-4451

References

Adebahr, B., Krause, M., Klein, U., Heald, G., & Dettmar, R.-J. 2017, A&A, 608, A29
Andersson, B.-G., Lazarian, A., & Vaillancourt, J. E. 2015, ARA&A, 53, 501
Beck, R. 2015, A&ARv, 24, 4
Beck, R., & Wielebinski, R. 2013, in Planets, Stars and Stellar Systems, Galactic Structure and Stellar Populations, Vol. 5, ed. T. D. Oswalt & G. Gilmore (Dordrecht: Springer), 641
Bertone, S., Vogt, C., & Enßlin, T. 2006, MNRAS, 370, 319
Bolatto, A. D., Warren, S. R., Leroy, A. K., et al. 2013, Natur, 499, 450
Boselli, A., Ciesla, L., Cortese, L., et al. 2012, A&A, 540, A54
Brevik, J. A. 2012, PhD thesis, California Institute of Technology
Bustard, C., Zweibel, E. G., & Cotter, C. 2017, ApJ, 835, 72
Cabral, B., & Leedom, L. C. 1993, in Proc. XX Annual Conf. Computer Graphics and Interactive Techniques, SIGGRAPH 93, ed. (New York: ACM), 263
Chandrasekhar, S., & Fermi, E. 1953, ApJ, 118, 113
Chevalier, R. A., & Clegg, A. W. 1985, Natur, 317, 44
Chuss, D. T., Andersson, B.-G., Bally, J., et al. 2018, ApJ, submitted
Chuss, D. T., Dowell, C. D., Hildebrand, R. H., & Novak, G. 2005, in ASP Conf. Ser. 343, Astronomical Polarimetry: Current Status and Future Directions, ed. A. Adamson et al. (San Francisco, CA: ASP), 311
Davidge, T. J. 2008, AJ, 136, 2502
de Cea del Pozo, E., Torres, D. F., & Rodriguez Marrero, A. Y. 2009, ApJ, 698, 1054
de Vaucouleurs, G. 1958, ApJ, 127, 487
Dowell, C. D., Cook, B. T., Harper, D. A., et al. 2010, Proc. SPIE, 7735, 77356H
Draine, B. T., & Lee, H. M. 1984, ApJ, 285, 89
Engelbracht, C. W., Kundurthy, P., Gordon, K. D., et al. 2006, ApJL, 642, L127
Everett, J. E., Zweibel, E. G., Benjamin, R. A., et al. 2008, ApJ, 674, 258
Förster Schreiber, N. M., Genzel, R., Lutz, D., & Sternberg, A. 2003, ApJ, 599, 193
Fujita, A., Martin, C. L., Mac Low, M.-M., New, K. C. B., & Weaver, R. 2009, ApJ, 698, 693
Greaves, J. S., Holland, W. S., Jenness, T., & Hawarden, T. G. 2000, Natur, 404, 732
Greco, J. P., Martini, P., & Thompson, T. A. 2012, ApJ, 757, 24
Griffin, M. J., Abergel, A., Abreu, A., et al. 2010, A&A, 518, L3
Harper, D. A., Jr., & Low, F. J. 1973, ApJL, 182, L89
Harper, D. A., Runyan, M. C., Dowell, C. D., et al. 2018, JAI, in press
Heesen, V., Krause, M., Beck, R., & Dettmar, R.-J. 2009, A&A, 506, 1123
Helou, G., Soifer, B. T., & Rowan-Robinson, M. 1985, ApJL, 298, L7
Hildebrand, R. H. 1983, QJRAS, 24, 267
Hildebrand, R. H., Dotson, J. L., Dowell, C. D., Schleuning, D. A., & Vaillancourt, J. E. 1999, ApJ, 516, 834
Hildebrand, R. H., Kirby, L., Dotson, J. L., Houde, M., & Vaillancourt, J. E. 2009, ApJ, 696, 567
Hopkins, P. F., Quataert, E., & Murray, N. 2012, MNRAS, 421, 3522
Houde, M., Hull, C. L. H., Plambeck, R. L., Vaillancourt, J. E., & Hildebrand, R. H. 2016, ApJ, 820, 38
Jones, T. J. 1989, ApJ, 346, 728
Jones, T. J. 1993, ApJ, 403, 135
Jones, T. J. 2000, AJ, 120, 2920
Jones, T. J., Bagley, M., Krejny, M., Andersson, B.-G., & Bastien, P. 2015, AJ, 149, 31
Jones, T. J., & Whittet, D. C. B. 2015, in Polarimetry of Stars and Planetary Systems, Vol. 147, ed. L. Kolokolova et al. (Cambridge: Cambridge Univ. Press)
Kaneda, H., Ishihara, D., Suzuki, T., et al. 2010, A&A, 514, A14
Karachentsev, I. D., & Kashibadze, O. G. 2006, Ap, 49, 3
Kobulnicky, H. A., Molnar, L. A., & Jones, T. J. 1994, AJ, 107, 1433
Kronberg, P. P., Lesch, H., & Hopp, U. 1999, ApJ, 511, 56
Krumholz, M. R., Burkhart, B., Forbes, J. C., & Crocker, R. M. 2018, MNRAS, 477, 2716
Larkin, J. E., Graham, J. R., Matthews, K., et al. 1994, ApJ, 420, 159
Lim, S., Hwang, N., & Lee, M. G. 2013, ApJ, 766, 20
Martini, P., Leroy, A. K., Mangum, J. G., et al. 2018, ApJ, 856, 61
Matthews, B. C., McPhee, C. A., Fissel, L. M., & Curran, R. L. 2009, ApJS, 182, 143
Morris, M. 2006, JPhCS, 54, 1
Murray, N., Ménard, B., & Thompson, T. A. 2011, ApJ, 735, 66
Naylor, B. J., Bradford, C. M., Aguirre, J. E., et al. 2010, ApJ, 722, 668
Nikola, T., Herter, T. L., Vacca, W. D., et al. 2012, ApJL, 749, L19
Ohyama, Y., Taniguchi, Y., Iye, M., et al. 2002, PASJ, 54, 891
Pence, W. D. 1980, ApJ, 239, 54
Pérez-Beaupuits, J. P., Güsten, R., Harris, A., et al. 2018, ApJ, 860, 23
Pilbratt, G. L., Riedinger, J. R., Passvogel, T., et al. 2010, A&A, 518, L1
Planck Collaboration, Aghanim, N., Akrami, Y., et al. 2018, arXiv:1807.06212
Poglitsch, A., Waelkens, C., Geis, N., et al. 2010, A&A, 518, L2
Rekola, R., Richer, M. G., McCall, M. L., et al. 2005, MNRAS, 361, 330
Reuter, H.-P., Klein, U., Lesch, H., Wielebinski, R., & Kronberg, P. P. 1994, A&A, 282, 724
Rieke, G. H., Lebofsky, M. J., Thompson, R. I., Low, F. J., & Tokunaga, A. T. 1980, ApJ, 238, 24
Roussel, H., Wilson, C. D., Vigroux, L., et al. 2010, A&A, 518, L66
Ruszkowski, M., Yang, H.-Y. K., & Zweibel, E. 2017, ApJ, 834, 208
Sharp, R. G., & Bland-Hawthorn, J. 2010, ApJ, 711, 818
Shopbell, P. L., & Bland-Hawthorn, J. 1998, ApJ, 493, 129
Spitzer, L. 1978, in Physical Processes in the Interstellar Medium, ed. L. Spitzer (New York: Wiley-Interscience), 333
Strickland, D. K., & Heckman, T. M. 2007, ApJ, 658, 258

Telesco, C. M. 1988, ARA&A, 26, 343
Telesco, C. M., Decher, R., & Joy, M. 1989, ApJL, 343, L13
Vaillancourt, J. E., Chuss, D. T., Crutcher, R. M., et al. 2007, Proc. SPIE, 6678, 66780D
Veilleux, S., Cecil, G., & Bland-Hawthorn, J. 2005, ARA&A, 43, 769
Walter, F., Bolatto, A. D., Leroy, A. K., et al. 2017, ApJ, 835, 265
Walter, F., Weiss, A., & Scoville, N. 2002, ApJL, 580, L21
Wardle, J. F. C., & Kronberg, P. P. 1974, ApJ, 194, 249
Yoast-Hull, T. M., Everett, J. E., Gallagher, J. S., III, & Zweibel, E. G. 2013, ApJ, 771, 73
Yoast-Hull, T. M., Gallagher, J. S., III, Zweibel, E. G., & Everett, J. E. 2014, ApJ, 780, 137
Yusef-Zadeh, F., Hewitt, J. W., & Cotton, W. 2004, ApJS, 155, 421
Zweibel, E. G. 1996, in ASP Conf. Ser. 97, Polarimetry of the Interstellar Medium, ed. W. G. Roberge & D. C. B. Whittet (San Francisco, CA: ASP), 486